Received: 1 March 2023 | Revised: 18 August 2023 | Accepted: 19 August 2023

DOI: 10.1002/cey2.469

RESEARCH ARTICLE

CARBON ENERGY WILEY

Self-supported VO_2 on polydopamine-derived pyroprotein-based fibers for ultrastable and flexible aqueous zinc-ion batteries

Jeong Seok Yeon[1] | Sul Ki Park[2] | Shinik Kim[3,4] | Santosh V. Mohite[3] | Won Il Kim[1] | Gun Jang[1] | Hyun-Seok Jang[5,6,7] | Jiyoung Bae[3] | Sang Moon Lee[8] | Won G. Hong[8] | Byung Hoon Kim[5,6,7] | Yeonho Kim[3] | Ho Seok Park[1]

[1]School of Chemical Engineering, College of Engineering, Sungkyunkwan University, Gyeonggi-do, Republic of Korea

[2]Department of Engineering, University of Cambridge, Cambridge, UK

[3]Department of Applied Chemistry, Konkuk University, Chungju, Republic of Korea

[4]Department of Chemistry, Ulsan National Institute of Science and Technology (UNIST), College of Natural Sciences, Ulsan, Republic of Korea

[5]Department of Physics, Incheon National University, Incheon, Republic of Korea

[6]Intelligent Sensor Convergence Research Center, Incheon National University, Incheon, Republic of Korea

[7]Institute of Basic Science, Incheon National University, Incheon, Republic of Korea

[8]Division of Material Analysis and Research, Korea Basic Science Institute, Daejeon, South Korea

Correspondence
Byung Hoon Kim, Department of Physics, Incheon National University, Incheon 22012, Republic of Korea.
Email: kbh37@inu.ac.kr

Yeonho Kim, Department of Applied Chemistry, Konkuk University, 27478 Chungju, Republic of Korea.
Email: yeonho@kku.ac.kr

Ho Seok Park, School of Chemical Engineering, College of Engineering, Sungkyunkwan University, 2066, Seobu-ro, Jangan-gu, Suwon-si, 440-746 Gyeonggi-do, Republic of Korea.
Email: phs0727@skku.edu

Funding information
National Research Foundation of Korea, Grant/Award Numbers: 2023R1A6A1A06084126, NRF-2021R1F1A1064111; Ministry of

Abstract

A conventional electrode composite for rechargeable zinc-ion batteries (ZIBs) includes a binder for strong adhesion between the electrode material and the current collector. However, the introduction of a binder leads to electrochemical inactivity and low electrical conductivity, resulting in the decay of the capacity and a low rate capability. We present a binder- and conducting agent-free VO_2 composite electrode using in situ polymerization of dopamine on a flexible current collector of pyroprotein-based fibers. The as-fabricated composite electrode was used as a substrate for the direct growth of VO_2 as a self-supported form on polydopamine-derived pyroprotein-based fibers (pp-fibers@VO_2(B)). It has a high conductivity and flexible nature as a current collector and moderate binding without conventional binders and conducting agents for the VO_2(B) cathode. In addition, their electrochemical mechanism was elucidated. Their energy storage is induced by Zn^{2+}/H^+ coinsertion during discharging, which can be confirmed by the lattice expansion, the formation of by-products including $Zn_x(OTf)_y(OH)_{2x-y}{\cdot}nH_2O$, and the reduction of V^{4+} to V^{3+}. Furthermore, the assembled

Jeong Seok Yeon, Sul Ki Park, and Shinik Kim contributed equally to this work.

Education, Grant/Award Number: NRF-2017R1A6A1A06015181

Zn//pp-fibers@VO_2(B) pouch cells have excellent flexibility and stable electrochemical performance under various bending states, showing application possibilities for portable and wearable power sources.

KEYWORDS
aqueous battery, binder free, conducting agent-free, flexible electrode, zinc-ion battery

1 | INTRODUCTION

Among the various energy storage systems, lithium-ion batteries (LIBs) have been considered promising candidates because of their high energy density and versatility in a wide range of applications.[1,2] However, the shortage of Li metal and its high cost and safety problems can lead to limitations in large-scale storage energy systems. As alternatives, rechargeable zinc-ion batteries (ZIBs), which consist of more abundant Zn metal, are receiving much attention due to their higher safety and lower cost than LIBs.[3,4] Despite the advantages, one critical issue is the development of high-capacity cathode materials for ZIBs.[5] Several cathode materials, such as manganese oxide and Prussian blue analogs, still exhibit a limited capacity of 250 and 120 mAh g^{-1}, respectively.[6–8] On the other hand, monoclinic vanadium dioxides (VO_2(B)) are large enough to enable the access of Zn ions easily because of the layered structure formed by the edge-sharing VO_6 octahedra with cavities.[9,10] It can deliver a higher capacity (>300 mAh g^{-1}) compared to other cathode materials.[11] However, VO_2 tends to dissolve in an aqueous Zn-ion electrolyte due to the strong polarity of H_2O and poor adhesion between VO_2 and the current collector, resulting in inferior cycling stability.[12,13]

Inspired by the adhesive nature of mussel adhesive proteins, dopamine is a promising material that can modify the surface properties of various substrates.[14] In addition, the in situ polymerization of dopamine on the fiber provides versatile adhesion properties, leading to the achievement of a layered and uniform coating of conducting carbon on the fiber after carbonization,[15] facilitating the homogeneous growth of active materials on the substrate. Recent studies have examined the beneficial role of polydopamine-derived carbon layers in enhancing the stability of cathode electrodes.[16] In addition, a homogeneous coating by in situ polymerization of dopamine can improve the adhesion properties of a substrate. Therefore, the combination strategy of a polydopamine-derived current collector and VO_2 electrode can prevent the dissolution of VO_2 without any binders and chemicals.

Apart from the active materials (e.g., VO_2(B)), the typical composite electrodes are composed of a binder and the current collector, where the active material can be adhered to the current collector by weak van der Walls force.[17,18] However, this configuration leads to many problems for ZIBs: (1) The introduction of a binder limits ion diffusion and mass transport due to its properties such as electrochemical inactivity and low conductivity; (2) the detachment of a binder from the current collector can be easily caused by their degradation and agglomeration during cycling.[19–21] These eventually result in a low rate capacity and cycle stability. Therefore, a binder-free electrode is required to overcome several problems mentioned earlier.

Here, we report a free-standing and flexible composite electrode system composed of self-supported VO_2(B) nanosheets along with polydopamine-derived pyroprotein-based fibers (pp-fibers@VO_2(B)) without binders and conducting agents. The VO_2(B) nanosheets were grown uniformly on pp-fibers through a facile hydrothermal method. The as-prepared products were used as the cathode for ZIBs without additional electrode fabrication processes. The cathode exhibits a superior electrochemical performance because of the following reasons: (1) the strong adhesion between the VO_2(B) and pp-fibers as the active materials and current collector, respectively, which prevents the dissolution of VO_2 and enables superior cycle stability; (2) the electrical conductivity and mass transportation of the electrode increase for not using binders and conducting agents. Furthermore, the Zn-ion storage mechanism of the pp-fibs@VO_2(B) electrode was systematically investigated through in situ and ex situ X-ray analysis techniques. The fabricated Zn//pp-fibers@VO_2(B) pouch cells show excellent flexibility and stable electrochemical performance under various bending states, indicating promising candidate possibilities for portable and wearable power sources.

2 | EXPERIMENTAL

2.1 | Synthesis of pp-fibers@VO_2(B)

First, 0.306 g of dopamine hydrochloride was dissolved in 50 mL of deionized water (D.I. water) under magnetic

stirring. Commercial silk (10 cm × 10 cm) was placed into the above solution, and then another 50 mL of D.I. water containing 0.855 g of sodium periodate was added. After stirring for 12 h at the ambient condition, polydopamine-coated silk (c-Silk@PDA) was washed with D.I. water three times and dried at 60°C. The c-Silk@PDA was annealed in a tube furnace in an argon atmosphere at 800°C for 3 h. The polydopamine structure breaks down around 300°C (Figure S2) and forms conducting nitrogen-doped carbon-derived pp-fibers electrode at 800°C. The resulting material is referred to as polydopamine-derived pyroprotein-based fibers, abbreviated as pp-fibers. Then, pp-fibers were placed in the solution containing 0.690 g of ammonium metavanadate (99.95% trace metals basis; Sigma-Aldrich) and 1.64 mL of formic acid with 60 mL of D.I. water for the synthesis of pp-fibers@VO_2(B). The above solution was then loaded into a Teflon-lined stainless-steel autoclave, placed in a preheated oven at 200°C for 48 h and cooled to room temperature. As-obtained pp-fibers@VO_2(B) was washed with D.I. water three times and dried at 50°C (loading mass of VO_2(B) on pp-fibers is 6–7 mg cm^{-2}). VO_2(B) was synthesized without adding pp-fibers, according to the same procedure.

2.2 | Materials characterizations

The morphologies of samples were investigated by field-emission scanning electron microscopy (SEM) (LEO SUPRA 55, GENESIS 2000 model) and high-resolution transmission electron microscopy (HR-TEM, JEM-2100F). Raman spectroscopy with a laser beam wavelength of 532 nm (inVia Raman microscopes) and X-ray photoelectron spectroscopy (XPS) were analyzed by micro X-ray/UV photoelectron spectrometer (AXIS-NOVA and Ultra DLD). The X-ray diffraction (XRD) was measured through a PanAlytical System in the 2θ range of 5°–90°. In situ XRD measurements were conducted in soft-packing Zn//pp-fibers@VO_2(B) batteries with polyimide film window fabricated by using the pp-fibers@VO_2(B) as cathode, Zn foil as anode, and 3 M $Zn(OTf)_2$ as electrolyte. Galvanostatic charge–discharge (GCD) curves of pouch batteries for in situ XRD were measured in a voltage range of 0.2–1.8 V by using a VMP3 potentiostat/galvanostat (Bio-Logic Co., Ltd.). In situ V K-edge X-ray absorption near-edge structure (XANES) measurement was conducted at beamline BL10C (Wide-XAFS) in the Pohang Accelerator Laboratory (PLS-II) using a Si(111) double-crystal monochromator, detuned to 70% of its original maximum intensity to eliminate high-order harmonics, and XANES data were handled using Athena software.

2.3 | Electrochemical measurements

2032-type coin cells were assembled with pp-fibers@VO_2(B) electrode, glass fiber separator (grade GF/A, pore size: 1.6 μm; Whatman), Zn foil (thickness: 0.1 mm, 99.98% trace metals basis; Sigma-Aldrich), and 3 M zinc trifluoromethanesulfonate electrolyte ($Zn(OTf)_2$, 98%; Sigma-Aldrich). Zn foil was washed with ethanol before use. VO_2(B) on coated Ti foil (Ti-VO_2(B) electrodes was also prepared to compare with pp-fibers@VO_2(B). The Ti-VO_2(B) electrode was prepared by mixing 80 wt% VO_2(B) as an active material, 10 wt% of a carbon black as a conductive agent, and 10 wt% polyvinylidene difluoride as a binder. The slurry was coated on Ti-foil (thickness: 0.06 mm, 99.7% trace metals basis; Sigma-Aldrich) using a doctor blade and dried at 80°C overnight in the vacuum oven (coating thickness: 80 μm) (Figure S8A,B). The coated Ti-foil was cut into circles with a diameter of 15 mm (loading mass of VO_2(B) on Ti foil is 6–7 mg cm^{-2}). The cyclic voltammetry (CV) curves were obtained using a VMP3 potentiostat/galvanostat (Bio-Logic Co., Ltd.). Electrochemical impedance spectroscopy (EIS) measurements were performed with a VMP3 potentiostat/galvanostat (Bio-Logic Co., Ltd.) in the frequency range of 10^6–10^{-1} Hz. The GCD profiles were measured on a Series4000 automated test system cell tester between 0.2 and 1.8 V at different current densities from 0.2 to 10.0 A g^{-1}. The electrochemical window of the Ti foil and pp-fiber as a working electrode was evaluated by linear sweep voltammetry curves in a three-electrode configuration, using Zn metal as the counter and reference electrode. The galvanostatic intermittent titration technique (GITT) measurement was conducted in a voltage window between 0.2 and 1.8 V at 0.2 C with a GCD pulse of each 2 min long, followed by 20 min of relaxation time. The soft-packing Zn//pp-fibers@VO_2(B) pouch cells were fabricated using the pp-fibers@VO_2(B) electrode (3 cm × 4 cm, 7.3 mg cm^{-2}, 140-μm thickness) as cathode, and Zn electrodeposited carbon felt as anode, and 3 M Zn $(OTf)_2$ as electrolyte. Zn electrodeposited on carbon felt was prepared with a three-electrode system by soaking pristine carbon felt (3 cm × 4 cm) as working electrode and Zn foil as counter and reference electrode in 2 M $ZnSO_4$ + 0.5 M Na_2SO_4 as an electrolyte in the beaker cell. Then, Zn has been electrically deposited on the carbon felt at a constant voltage of −1.0 V for 5 min.

3 | RESULTS AND DISCUSSION

The pp-fibers@VO_2(B) was prepared by a wet-chemical synthetic method including an in situ polymerization process. Compared to the pristine pyroprotein-based

fibers, our pp-fibers show a higher flexibility and electrical conductivity after the pyrolysis process. However, the pyroprotein-based fibers were deformed during the high-temperature pyrolysis process without the polydopamine coating (Figure S1). The spontaneous self-polymerization of dopamine and π–π stacking interactions in polydopamine molecules preserve the structure and integrity of pp-fibers and their arrays.[22] During the pyrolysis process under Ar, the organic components of polydopamine undergo decomposition (Figure S2). This decomposition process leads to the formation of carbonaceous residues. Subsequently, these residues undergo carbonization, where the remaining carbon atoms reorganize and form a nitrogen-doped carbon network.[16] The pyrolysis process results in the formation of carbonaceous residues that preserve the structure of the pyroprotein-based fibers.

The pp-fibers surface is very smooth and clean (Figure S3). It has a surface area of 124.78 $m^2 g^{-1}$, a pore volume of 0.06 $cm^3 g^{-1}$, and an average pore diameter of 2.05 nm (Figure S4 and Table S1). In contrast, the pp-fibers@VO_2(B) has a non-smooth surface, with randomly grown VO_2(B) nanosheet on the pp-fibers (Figure 1C). The average pore diameter (20.59 nm) of pp-fibers@VO_2(B) increased due to the numerous VO_2(B) nanosheets assembled into an interconnected open porous structure. Thus, composite electrodes can provide an accessible surface area (5.82 $m^2 g^{-1}$) for the electrolyte when used as a cathode for ZIBs. The high-magnification SEM image of the pp-fibers@VO_2(B) shows that the thickness of a VO_2(B) nanosheet is ranged from 30 to 200 nm (Figure S5). Figure 1D presents an HR-TEM image in which interplanar distances of 0.29, 0.35, and 0.57 nm are assigned to the (002), (110), and (200) planes of VO_2(B), respectively.[23] In addition, the growth of VO_2 on pp-fibers (Figure S6) and commercial carbon cloths (Figure S7) can be revealed from SEM image and energy-dispersive X-ray spectroscopy (EDS) elemental maps. It is observed that VO_2 is uniformly grown onto the pp-fibers compared to the commercial carbon cloths. This is a significant advantage as a large quantity of the active materials can be loaded onto the pp-fibers. The elemental compositions of VO_2 on pp-fibers and carbon cloths in at % are summarized in Table S2. EDS maps of the pp-fibers@VO_2(B) clearly exhibit a uniform distribution of the C, V, and O elements, indicating a random distribution of VO_2 on the pp-fibers' surface (Figure 1E–H).

Titanium (Ti) foil, often used as typical current collectors for ZIBs, has the disadvantages of high cost and low flexibility (Figure S8).[24] The Ti foil consistently displayed distinct crease marks throughout the bending tests, underscoring its poor flexibility. However, the modified pp-fibers electrode exhibits outstanding

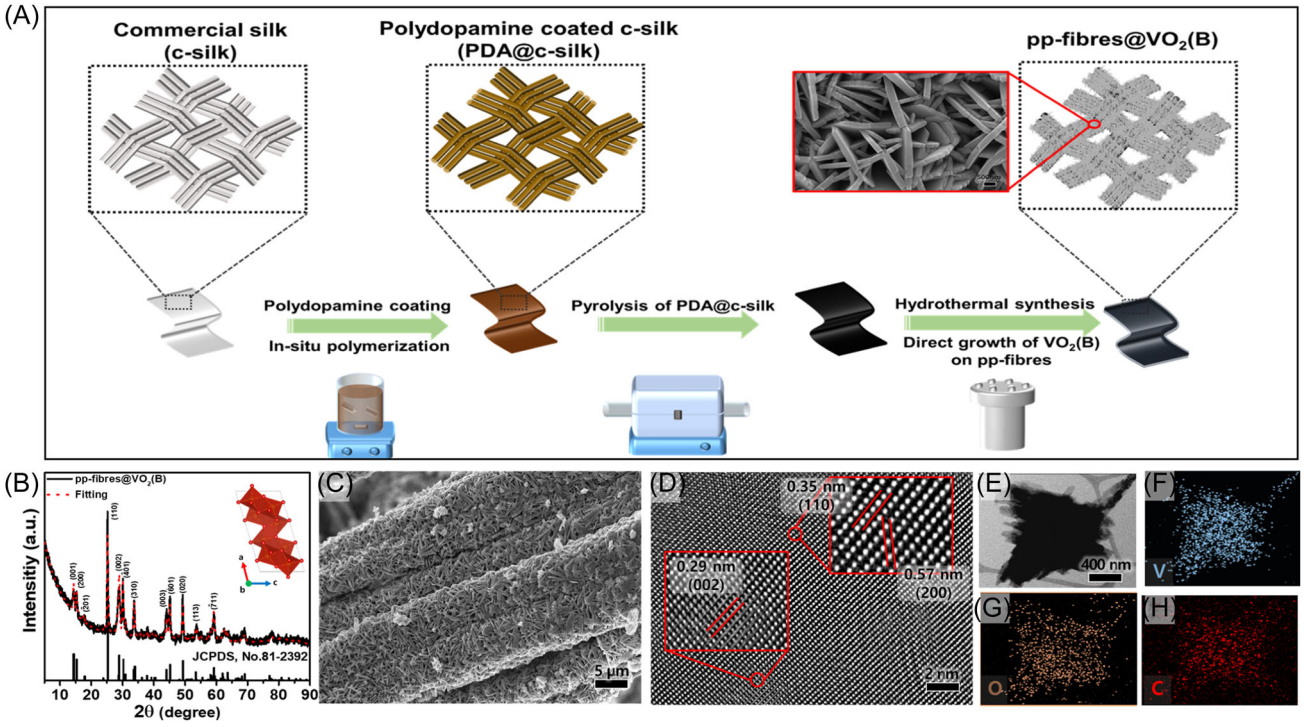

FIGURE 1 (A) Schematic illustration for the preparation of the pp-fibers@VO_2(B) composite. (B) XRD patterns, (C) low-magnification SEM image, and (D, E) TEM images of the as-obtained pp-fibers@VO_2(B). (F–H) EDS elemental maps of V, O, and C elements of pp-fibers@VO_2(B).

mechanical properties, including flexibility and bending characteristics, as depicted in Figure S9. Therefore, the pp-fibers can be utilized to easily fabricate a flexible current collector in low cost.[25] The pp-fibers also exhibit better electrochemical stability in an aqueous electrolyte compared with a carbon felt (Figure S10). In addition, pp-fiber-based electrode exhibits better electrolyte wetting than the conventional slurry-coated electrode on Ti foil (Figure S11); this results in lower interfacial resistance for pp-fiber@VO_2(B), which will be discussed later. The pp-fibers substrate provides negligible capacity in the ZIB systems but only serves as a highly conductive and flexible current collector to improve the active material performance (Figure S12). In this experiment, the pp-fibers@VO_2(B) was used as a cathode to configure full aqueous ZIBs with Zn metal as an anode in 3 M $Zn(OTf)_2$ electrolyte, which is more stable and efficient than the elctrolyte with the concentration ranging in 1–2 M (Figure S13). Notably, the 3D surface of VO_2(B) on pp-fibers is proved advantageous in establishing extensive electrochemical contact with the electrolyte, as elucidated by X-ray microscopy analysis (Figure S14). This distinctive structure enables a significant surface area to come into contact with the electrolyte, facilitating substantial electrolyte penetration due to the material's inherent porosity and three-dimensional (3D) surface architecture. Consequently, the combination of the 3D surface and porous nature of the pp-fibers@VO_2(B) ensures a large active material surface available for redox reactions. In addition, the abundant N heteroatoms formed on the pp-fibers during the thermal treatment process provide an improved electrical conductivity to directly grown VO_2(B) as well as a strong interaction between the pp-fibers and VO_2(B), thereby improving the rate capability and cycle stability (Figure S15).

The electrochemical behavior of the pp-fibers @VO_2(B) as a cathode in a ZIB system was investigated between 0.2 and 1.8 V versus Zn/Zn^{2+} at 0.1 mV s^{-1}. The electrochemical behavior and performance were evaluated by CV and the GCD. As shown in CV curves (Figure 2A), the initial five cycles of the CV profiles of the pp-fibers@VO_2(B) are nearly overlapped, suggesting the reversibility in the Zn//pp-fibers@VO_2(B) ZIB configuration. The distinct two pairs of reduction/oxidation peaks at 0.48/0.72 and 0.89/1.14 V are associated with the Zn^{2+} storage mechanism of the pp-fibers@VO_2(B), which confirmed a multiple-step (de)insertion process.[26] In contrast, the VO_2(B) coated on the Ti foil, used as an electrode, had no redox peaks in the initial cycle (Figure S16). On consecutive cycles, the two pairs of redox peaks appeared and gradually increased by successive cycling, which is attributed to the activation process of

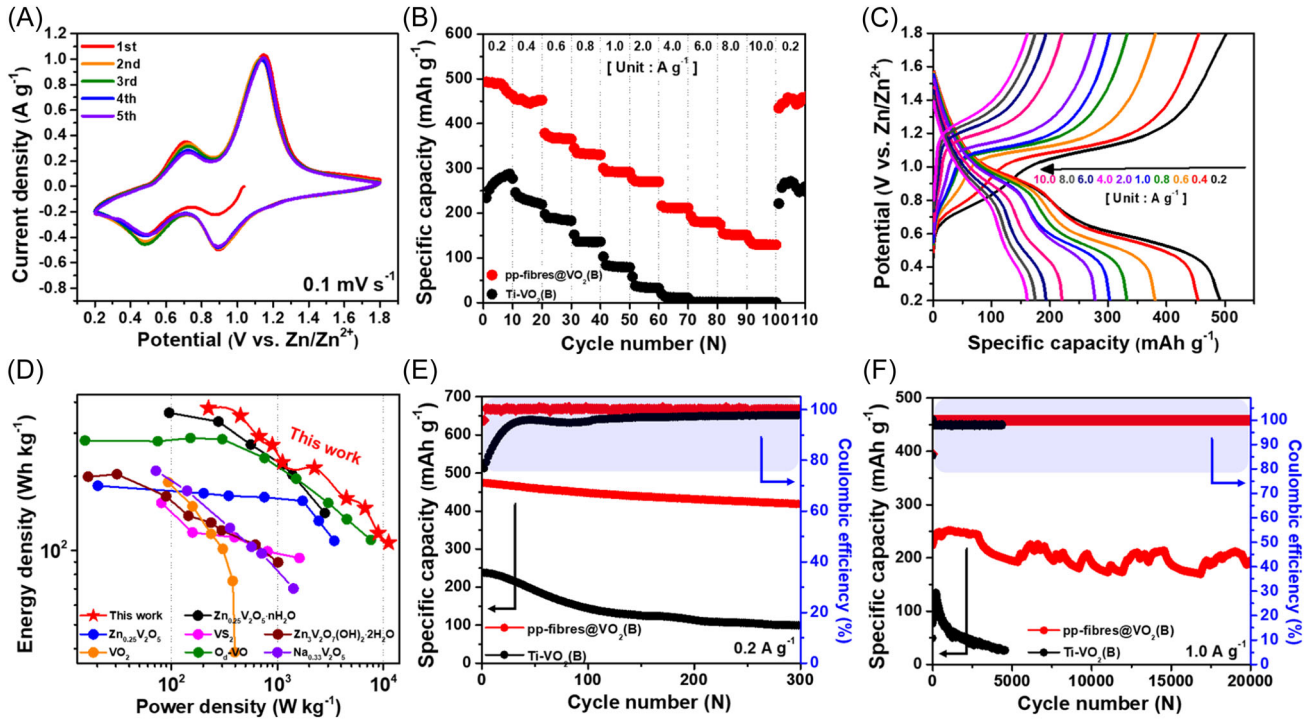

FIGURE 2 (A) CV curves of pp-fibers@VO_2(B). (B) Rate performance with current densities from 0.2 to 10.0 A g^{-1} of pp-fibers@VO_2(B) in comparison with Ti-VO_2(B). (C) GCD curves of pp-fibers@VO_2(B) at various current densities from 0.2 to 10.0 A g^{-1}. (D) Comparison of the Ragone plot of the Zn//pp-fibers@VO_2(B) battery with reported vanadium-based ZIBs.[7,22–27] (E) Cycling performance at 0.2 A g^{-1} and (F) long-term cycling properties of pp-fibers@VO_2(B) in comparison with Ti-VO_2(B) at 1.0 A g^{-1}.

the VO_2(B) due to its poor electrical conductivity and electrolyte wetting.[27] The GCD profiles of the pp-fibers@VO_2(B) at 0.2 A g^{-1} are shown in Figure S17. Two distinct plateaus are observed in the GCD profiles, which are consistent with CV profiles in Figure 2A, indicating that the Zn^{2+} storage mechanism of the pp-fibers@VO_2(B) is based on a multiple (de)intercalation process.[28] An initial specific discharge capacity of 491 mAh g^{-1} is achieved, which presents a much higher specific capacity than those of the previously reported vanadium-based electrodes (Table S3). The GCD profiles coincide well with the initial 10 profiles, demonstrating excellent reversibility and stability.

The rate capability of the Zn//pp-fibers@VO_2(B) based ZIBs was investigated at different current densities from 0.2 to 8.0 A g^{-1} (Figure 2B). The pp-fibers@VO_2(B) cathode delivers the high specific capacities of 491, 458, 377, 348, 296, 281, 211, 193, and 153 mAh g^{-1} at 0.2, 0.4, 0.6, 0.8, 1.0, 2.0, 4.0, 6.0, and 8.0 A g^{-1}, respectively. Even at a high specific current of 10.0 A g^{-1}, the pp-fibers@VO_2(B) cathode exhibits a high-rate capacity of 140 mAh g^{-1}. After 100 cycles at different current densities, the specific capacity is recovered to 428 mAh g^{-1} at 0.2 A g^{-1}, suggesting that the pp-fibers@VO_2(B) cathode has outstanding reversibility. The typical GCD profiles of the pp-fibers@VO_2(B) corresponding to each of the applied current densities show that the plateaus of the GCD curves are well preserved even at a high specific current, indicating superb charge transfer kinetics (Figure 2C). On the other hand, for the VO_2(B) cathode, an initial capacity of 234 mAh g^{-1} was achieved at 0.2 A g^{-1}. Then, it gradually increased due to the activation process, as supported by the previous CV results (Figure S18A). As the current densities gradually increase from 0.4 to 8.0 A g^{-1}, VO_2(B) delivers lower specific capacities compared to pp-fibers@VO_2(B) at the same current densities, exhibiting significant polarization between the charge–discharge profiles (Figure S18B). The sharp difference between the electrochemical behaviors of the two cathodes indicates that the interconnected multichannel of the highly conductive pp-fibers framework can facilitate the electrochemical redox kinetics by providing VO_2(B) with both rapid percolated and continuous ion-conducting pathways.

As shown in Figure 2D, the Ragone plot also demonstrates the superior kinetic performance of the pp-fibers@VO_2(B) electrode compared with the other recently reported vanadium-based cathodes, such as $Zn_{0.25}V_2O_5{\cdot}nH_2O$,[29] $Zn_{0.25}V_2O_5$,[7] VS_2,[30] $Zn_3V_2O_7(OH)_2{\cdot}2H_2O$,[31] VO_2,[32] O_d-VO_2,[33] and $Na_{0.33}V_2O_5$.[34] The composites electrode of pp-fibers@VO_2(B) not only achieves a relatively high energy density of 378 Wh kg^{-1} at a power density of 227 W kg^{-1} but also still delivers an energy density of 108 Wh kg^{-1} at a superior power density of 11 kW kg^{-1} (based on the mass of the cathode). The cyclic performance of the pp-fibers@VO_2(B) at a low specific current of 0.2 A g^{-1} was investigated (Figure 2E). The pp-fibers@VO_2(B) cathode exhibits a stable cycling performance with a high initial discharge capacity of 490 mAh g^{-1}. After 300 cycles, a high capacity of 414 mAh g^{-1} can be retained at 84% of the initial capacity, corresponding to a capacity fading rate of 0.052% per cycle. For the VO_2(B), a low initial discharge capacity of 238 mAh g^{-1} is delivered, and the discharge capacity drastically decreases in consecutive cycles. After 300 cycles, the capacity retention is only 41%, corresponding to a capacity fading rate of 0.195% per cycle.

To further compare the electrochemical stability, the long-term cycling stability of the pp-fibers@VO_2(B) and VO_2(B) was measured at a high specific current of 1.0 A g^{-1} (Figure 2F). The capacity increased in the initial cycle at a high specific current due to the activation effect.[35] The pp-fibers@VO_2(B) cathode shows a stable cycling performance with an initial discharge capacity of 232 mAh g^{-1}. Even after 20,000 cycles at 1.0 A g^{-1}, the Zn-ion cell with the pp-fibers@VO_2(B) still delivers a high reversible discharge capacity of 186 mAh g^{-1}, corresponding to an imperceptible capacity fading rate of 0.001% per cycle. Moreover, at 6.0 A g^{-1}, the capacity fading rate was 0.0018% up to 11,000 cycles (Figure S19). By contrast, the maximum discharge capacity of the VO_2(B) was 137 mAh g^{-1} and dramatically decreased to 24 mAh g^{-1} after only 4500 cycles (capacity fading rate of 0.0196% per cycle).

The morphological changes of the pp-fibers@VO_2(B) cathode were investigated by SEM to prove the structural integrity of the cycled electrode (Figure S20). After 300 cycles at 0.2 A g^{-1}, the morphology of the pp-fibers@VO_2(B) was well maintained without any obvious structural deformation relative of the initial state, which confirms the remarkable structural stability for the composites electrode of pp-fibers@VO_2(B).[36]

To further understand the structural changes of the pp-fibers@VO_2(B) cathode involved in the charge/discharge processes, electrochemical in situ XRD analysis was conducted during the first cycling process at a specific current of 0.2 A g^{-1} (Figure 3A). The in situ XRD patterns (Figure 3B,C of the pp-fibers@VO_2(B) show peak ranges of 6°–6.6°, 2.5°–15.5°, 16°–35°, and 42°–62°, respectively. The crystal planes corresponding to each diffraction peak are marked at the top of the patterns. Upon discharging, the overall peaks of the VO_2(B) continuously shift to a lower degree, indicating an increase in the interlayer distance of the VO_2(B) framework, which is caused by Zn^{2+} insertion. The lattice parameters of the VO_2(B) were refined by the

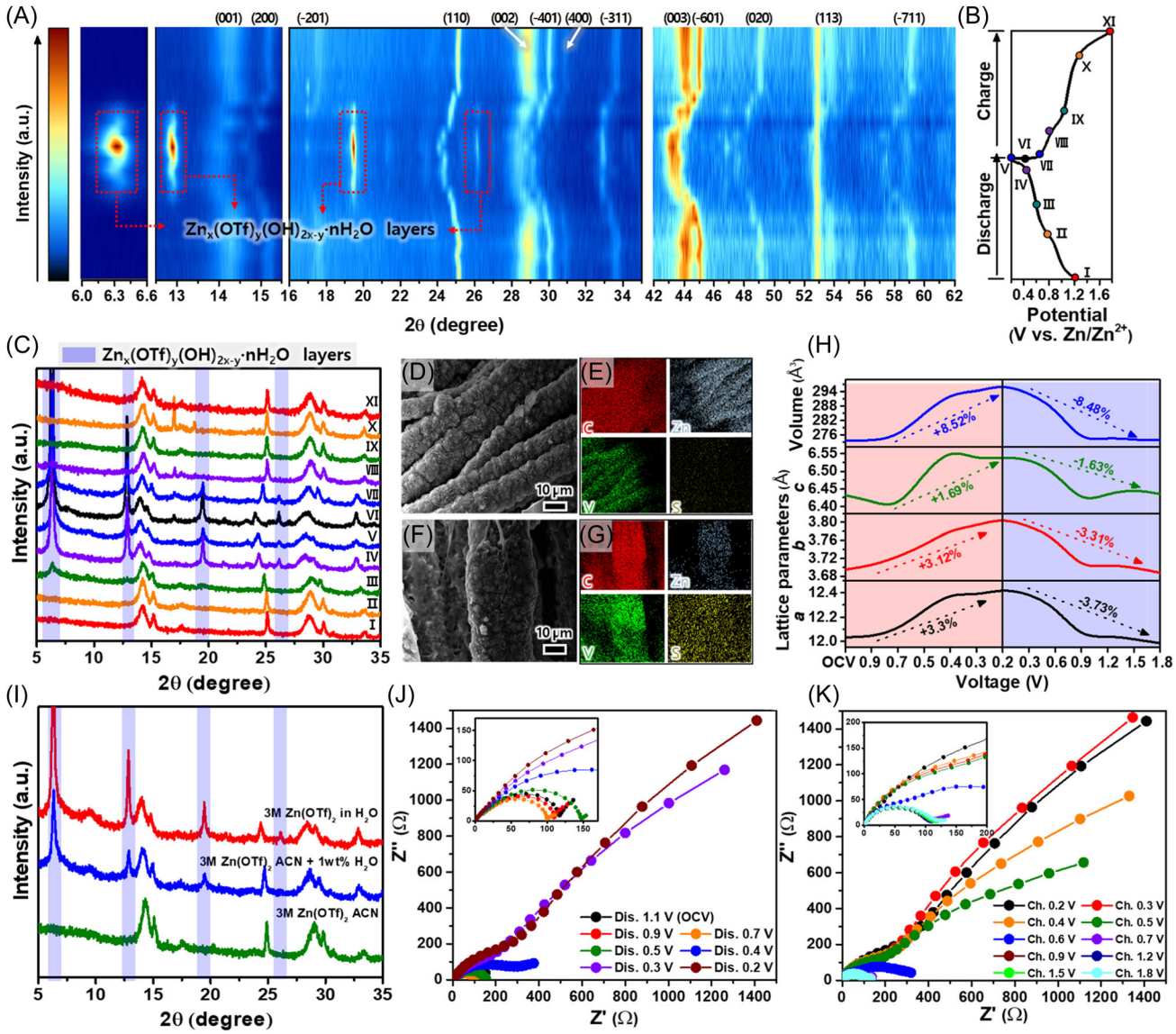

FIGURE 3 (A) Two-dimensional contour plots of the in situ XRD patterns collected in the first cycle at 0.2 A g^{-1} and (B) corresponding discharge/charge profiles of pp-fibers@VO_2(B). (C) In situ XRD patterns of pp-fibers@VO_2(B) at various discharge/charge states. SEM images and EDS elemental maps of discharged state pp-fibers@VO_2(B) at (D, E) 0.5 V and (F, G) 0.2 V. (H) The evolution of lattice parameters and unit-cell volume during the discharge–charge process. (I) Ex situ XRD patterns of fully discharged states of pp-fibers@VO_2(B) according to three types of electrolytes. EIS spectra at different electrochemical states during the (J) discharge and (K) charge process.

Rietveld method. Interestingly, four peaks located at 6.4°, 12.8°, 19.6°, and 26.1° newly appeared and gradually strengthened upon discharging from 0.5 to 0.2 V. These four peaks can be attributed to the formation of the zinc hydroxide triflate (ZHT; $Zn_x(OTf)_y(OH)_{2x-y}{\cdot}nH_2O$) precipitation (Figure 3B,C).[37] This result is well matched to the previously reported ZHT pattern.[38] This precipitate demonstrates the possibility of proton insertion. As shown in Figures 3D,F and S21, the SEM images of the electrode at the fully discharged state (0.2 V) are significantly different from those of the discharged state (0.5 V) because the ZHT layers form at the surface of the electrode below 0.5 V. The EDS data (discharged state at 0.2 V) further confirm that the surface of the electrode is covered by ZHT layers with a large amount of S and Zn elements (Figure 3G). In contrast, the S element is depleted at 0.5 V (Figure 3E). This further confirms that the proton storage process of the VO_2(B) occurred between 0.5 and 0.2 V during the discharge process. In the following charging process, the new peaks disappear from 0.2 to 0.5 V, and the VO_2(B) phase returns to its original peak positions, indicating the high reversibility of the Zn^{2+}/H^+ (de)insertion process. The reversible structural changes upon the Zn^{2+}/H^+ insertion result in

a high capacity by providing an abundant Zn^{2+} storage site and the excellent long-term cycle stability of the Zn// pp-fibers@VO_2(B). The change in lattice parameters of the VO_2(B) during the charge/discharge processes was observed by the Rietveld method. After Zn^{2+}/H^+ insertion, each of the lattice parameters (*a*, *b*, and *c*) of the VO_2(B) was expanded by 3.30%, 3.12%, and 1.69%, respectively, and the unit-cell volume increased by 8.52% compared to the pristine state (Figure 3H). Upon Zn^{2+}/H^+ extraction, both the lattice parameters (*a*, *b*, and *c*) and the unit-cell volume present a pronounced reduction of about 3.73%, 3.31%, 1.63%, and 8.48%, respectively, demonstrating that the structural change of the pp-fibers@VO_2(B) is reversible during the Zn^{2+}/H^+ coinsertion reaction.

In general, ZHT layers are formed by hydroxyl ion (OH^-) and $Zn(OTf)_2$ aqueous electrolyte.[26] The OH^- ions, formed by the water decomposition reaction, react with the $(CF_3SO_3)_2^{2-}$ anions of the Zn salt in the electrolyte while the H^+ concentration increases. These H^+ ions are hard to exist in the electrolyte independently. As a result, H^+ could be inserted into the VO_2(B) electrode.[39] The pH of the electrolyte increases rapidly between 0.5 and 0.2 V (Figure S22), which is attributed to the H^+ insertion and supports the formation of the ZHT precipitation.

The structure of the pp-fibers@VO_2(B) electrode at the fully discharged state under different electrolyte media was characterized by XRD to demonstrate the structural changes caused by the insertion of the proton. As shown in Figure 3I, in a nonaqueous electrolyte, diffraction peaks are shifted to a lower angle due to the Zn^{2+} insertion, but no new peak appears. By contrast, in different nonaqueous electrolytes with 1 wt % H_2O, new diffraction peaks are observed in the XRD patterns of the VO_2(B). This suggests that the generated peaks are clearly related to the insertion H^+.[40] Thus, the storage of Zn^{2+}/H^+ can result in the composites electrode of pp-fibers@VO_2(B) having a higher capacity (Figure S23).

To further understand the reaction kinetics of the pp-fibers@VO_2(B) cathode, EIS measurements were conducted at different electrochemical states during the discharge process.[41] As shown in Figure 3J, the EIS spectra maintained a similar shape from the open-circuit voltage (OCV) to 0.7 V. However, the charge transfer resistance (R_{ct}) value slightly increases when the potential is close to 0.5 V. As the discharge potential went down further to 0.2 V, the impedance increased dramatically, showing a significant difference from that before 0.5 V. When the potential goes back to 1.8 V, R_{ct} value decreases to its initial value with a similar shape at the OCV states, implying good reversibility of the electrochemical reaction in the pp-fibers@VO_2(B) (Figure 3K). Surprisingly, even though insulating layers on the electrode surface formed, the ZHT precipitate showed high reversibility and long-term stability.

The composites electrode of pp-fibers@VO_2(B) cathode was prepared in the different charging states such as its pristine state, fully charged state at 1.8 V, and fully discharged state at 0.2 V to elucidate the Zn-ion storage mechanism. The XPS spectra of Figure S24A show that no Zn-related peaks are observed in the high-resolution Zn 2p region, representing no Zn component in the pristine state of the electrode. When the electrode is discharged to 0.2 V, two peaks are observed at 1045.2 eV (Zn $2p_{1/2}$) and 1022.1 eV (Zn $2p_{3/2}$), demonstrating the insertion of Zn^{2+} into the VO_2(B) framework.[42] When the electrode is charged to 1.8 V, the significant decrease of Zn peaks indicates the reversibility of the insertion/extraction process. However, some peaks remain, which could be attributable to residual Zn salt sediment or irreversibly absorbed Zn salt on the surface.[43]

CV profiles (Figure 4A), which were recorded under various scan rates from 0.1 to 1.5 mV s^{-1}, were investigated to understand the outstanding power performance for the composites electrode of pp-fibers@VO_2(B) cathode on ZIB. As the scan rate increases, two pairs of peaks in the oxidation and reduction states gradually shift toward higher and lower potentials, suggesting the presence of a typical surface-confined pseudocapacitive behavior.[44] The four peaks marked as A_1, A_2, C_1, and C_2 in Figure 4A could be described by the relationship between the current (i) and the scan rate (ν) in the CV profiles, as shown by the following power-law formula[45]:

$$i = a\nu^b, \tag{1}$$

where the b value is the key parameter for estimating the dominant storage process of the Zn ions between the capacitive-controlled ($b = 1.0$) and diffusion-controlled process ($b = 0.5$), which is determined by the slope of the corresponding $\log i$ versus $\log \nu$) plots. As shown in Figure 4B, b-values of A_1, A_2, and C_2 are calculated to be 0.835, 0.701, and 0.712, respectively, implying that the capacity of the pp-fibers@VO_2(B) is dominated by the surface-capacitive electrochemical reaction. On the other hand, the b value of C1 is lower at 0.510, indicating that the C_1 peak is dominated by a diffusion-controlled process, and most of the capacity at a high scan rate is dependent on the redox kinetics of the C_2 peak.[46]

The relative contribution of the capacitive- and diffusion-controlled processes are quantified by the following equation:[47]

$$i(\mathrm{V}) = k_1\nu + k_2\nu^{0.5}. \tag{2}$$

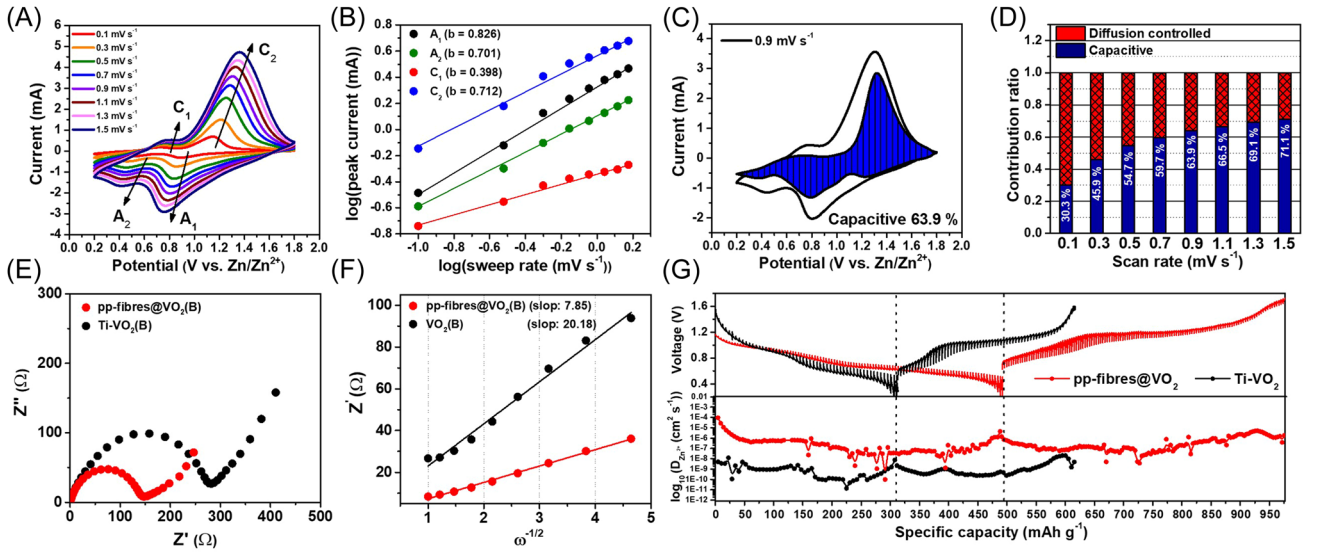

FIGURE 4 (A) CV curves measured at various scan rates of 0.1–1.5 mV s^{-1}. (B) Plots of log *i* versus log *ν* plots at each redox peak of pp-fibers@VO_2(B). (C) Capacitive contribution (blue-colored region) and diffusion contribution at 0.9 mV s^{-1}. (D) Contribution of capacitor-like and diffusion-controlled charge storage process of pp-fibers@VO_2(B) from 0.1 to 1.5 mV s^{-1}. (E) Nyquist plots for Zn-ion cells with pp-fibers@VO_2(B) and Ti-VO_2(B) cathode. (F) Relationships between the real resistance (*Z*′) and the inverse square root of angular speed ($\omega^{-1/2}$) in the low-frequency region for Zn-ion cells with pp-fibers@VO_2(B) and Ti-VO_2(B) cathode. (G) GITT analysis and the corresponding diffusivity coefficient (*D* value) of the Zn^{2+} at pp-fibers@VO_2(B) and Ti-VO_2(B) cathode, respectively.

Here, Equation (2) can be modified as follows:

$$i(\mathrm{V})/\nu^{0.5} = k_1\nu^{0.5} + k_2, \tag{3}$$

where the terms of $k_1\nu$ and $k_2\nu^{0.5}$ pertain to the capacitive- and diffusion-controlled processes, respectively. The linear relationship plots between $i(\mathrm{V})/\nu^{0.5}$ versus $\nu^{0.5}$, and then the value of k_1 and k_2 can be calculated by Equation (3). As shown in Figure 4C, 63.9% of the total capacity is dominated by the capacitive-controlled contribution at 0.9 mV s^{-1} (blue-colored region). With the increase in the scan rate, the ratio of the capacitive-controlled contribution at 0.1–1.5 mV s^{-1} gradually increases from 30.3 to 71.1, demonstrating that the high rate capability of the pp-fibers@VO_2(B) is associated with the surface pseudocapacitive behavior (Figure 4D).

The improved electrochemical performance was further investigated by EIS measurements (Figure 4E). Both electrodes show one semicircle in the high-frequency region and a straight line in the low-frequency region. The R_{ct} value of the pp-fibers@VO_2(B) was measured to be 145.1 Ω, which is much lower than that of VO_2(B) (281.80 Ω), indicating that the introduction of the pp-fibers can be a synergistic contribution to the electronic conductivity of VO_2. Figure 4F shows the linear relationship between the real impedance (*Z*′) and low-frequency region ($\omega^{-1/2}$) for the pp-fibers@VO_2(B) and VO_2(B), representing the solid-state Zn^{2+} diffusion within the bulk of the electrode. The linear slope suggests the degree of Zn^{2+} diffusion into the internal electrode.[48] The slope of the pp-fibers@VO_2(B) was calculated to be 7.85, which is lower than that of the VO_2(B) (20.18), further confirming the fast Zn^{2+} diffusion pathway provided by the porous pp-fibers framework.

The GITT was used to estimate the charge species (Zn^{2+}/H^+) diffusion coefficient in the pp-fibers@VO_2(B) (Figure 4G). The average diffusion coefficient values of the discharge and charge processes were measured to be 5.6×10^{-7} and 3.5×10^{-6} cm^2 s^{-1} in the working voltage window, respectively, which is much higher than those of the VO_2(B) cathode (1.3×10^{-9} and 2.4×10^{-9} for the diffusion coefficient value of the discharge and charge processes, respectively). This result further confirms that the pp-fibers@VO_2(B) enables rapid charge species migration into the electrodes, resulting in a superior rate capability.

For the high-resolution V 2p region (Figure 5A), the fitted V 2p of the pristine electrode is located at 523.7 (V $2p_{1/2}$) and 516.3 eV (V $2p_{3/2}$), corresponding to the V^{4+} species.[49] When the electrode is fully discharged to 0.2 V, the V^{4+} peaks are slightly weakened and shift to the high-binding-energy region, while new peaks appear at 522.9 and 515.9 eV, indicating the partial reduction of V^{4+} to V^{3+} due to the H^+/Zn^{2+} co-(de)insertion.[21] After

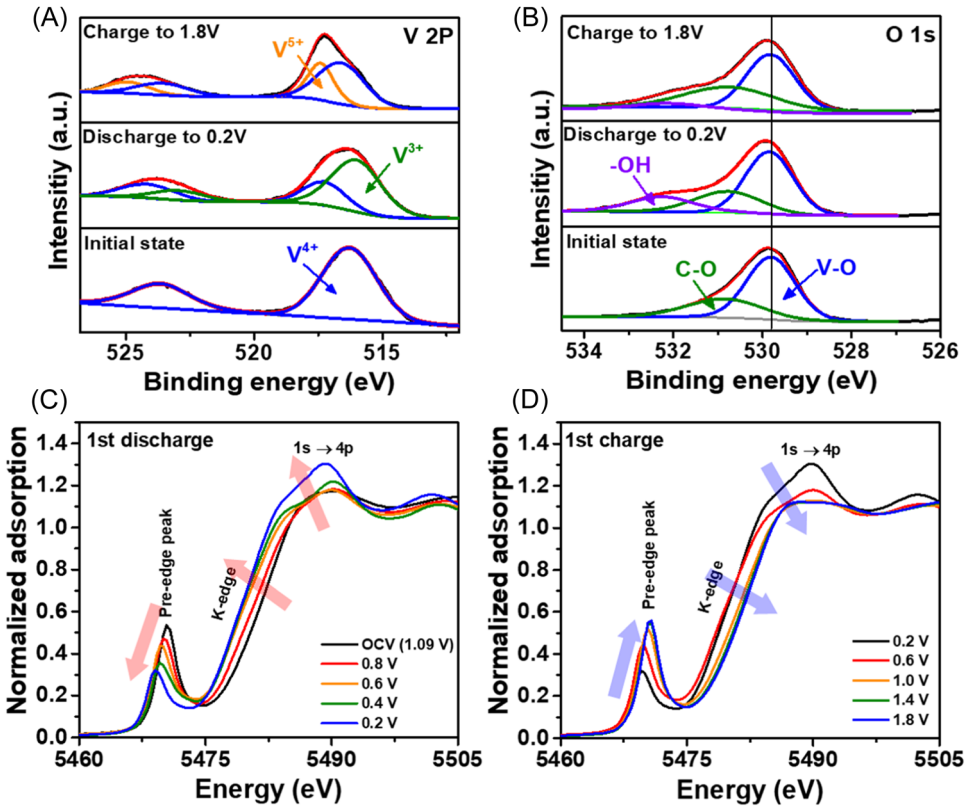

FIGURE 5 High-resolution XPS spectra of (A) V 2p and (B) O 1s in the initial- and fully discharged/charged states of pp-fibers@VO_2(B). The V K-edge in XANES of pp-fibers@VO_2(B) during (C) the first discharge and (D) the first charge process.

the electrode was fully charged to 1.8 V, the V 2p spectra returned to its original state as V^{4+} as well as partially further oxidized to V^{5+} state.[50] Meanwhile, the high-resolution O 1s region of the pristine state is divided into two peaks at 529.8 and 530.9 eV, which correspond to V–O and C–O, respectively (Figure 5B). The new peak at 532.3 eV related to –OH was found to increase after discharging process and decrease following charging process the existence and reversibility of the ZHT precipitation.[51] In addition, the formation and reversibility of the ZHT were also confirmed by the S 2p XPS spectra (Figure S24B), further suggesting that the electrochemical reaction of the pp-fibers@VO_2(B) cathode for the ZIB results from the coinsertion/extraction of the Zn^{2+} and H^+.[45]

To further demonstrate the changes in the valence state and local chemical environment of the VO_2(B) crystal, in situ XANES measurements were done on the pp-fibers@VO_2(B) electrode. The V K-edge XANES can be assigned to three regions: pre-edge (1s core level to 3d state), K-edge, and edge resonance (1s core level to 4p state).[52] In particular, the intensity of the pre-edge is sensitive to the local geometrical configurations, and it could be used to derive the structural and chemical information in the local geometrical symmetry of the V atoms qualitatively. Figure 5C shows the normalized V K-edge XANES spectra of the pp-fibers@VO_2(B) cathode during the discharge process. The K-edge of the V continuously shifted to the lower binding energy on the insertion of Zn ions, corresponding to a decrease in the average oxidation state of the V due to the insertion of the Zn^{2+}/H^+. In addition, the position of the pre-edge also shifted to lower values and its intensity weakened, indicating the weaker extent of the distortion of the monoclinic geometry in the VO_2(B). After the charging process, the K-edge and pre-edge of the V nearly recovered to the initial state, demonstrating the structural reversibility of the VO_2(B) (Figures 5D and S25).

To validate the practical feasibility of the pp-fibers@VO_2(B) electrode, Zn//pp-fibers@VO_2(B) pouch cells with an area of 12 cm^2 (3 cm in width × 4 cm in length) were assembled. Furthermore, to show the flexible characteristics of the pouch cells, carbon felt with electrically deposited Zn was used instead of Zn foil (Figure S26). As shown in Figure 6A, the GCD profiles of the Zn//pp-fibers@VO_2(B) pouch cells show similarity to those of the coin-type cell in the voltage range of 0.2–1.8 V. The GCD profiles under various bending states also exhibit a stable electrochemical behavior, showing excellent flexible properties and the possibility of

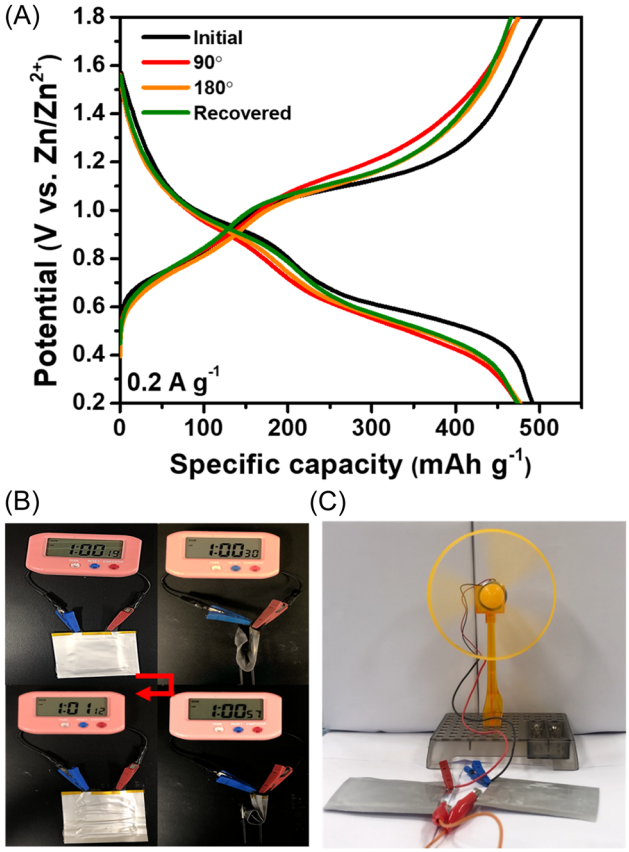

FIGURE 6 (A) GCD curves of Zn//pp-fibers@VO_2(B) at various bending states. Optical images of (B) a commercial electric timer powered by one device and (C) a commercial mini electric fan powered by two devices in series.

supplying a power source to practical wearable devices.[53–56] Furthermore, the practical applicability of the assembled pouch cells was demonstrated through the operation of an electric timer and a mini electric fan, revealing the ability of the Zn//pp-fibers@VO_2(B) pouch cells to provide a high energy output and serve as a power source under practical use (Figure 6B,C).

4 | CONCLUSIONS

In summary, this paper reported a novel approach to use polydopamine-derived pyroprotein-based fibers, pp-fibers, as a flexible current collector for aqueous ZIBs. Self-supported VO_2(B) nanosheets were grown uniformly on pp-fibers by a facile hydrothermal process and used directly as a cathode. In an aqueous $Zn(OTf)_2$ electrolyte, the reversible H^+/Zn^{2+} cointercalation mechanism was demonstrated by combining electrochemical measurements with various analytic techniques. In particular, it was demonstrated that the H^+ (de)insertion process is induced through the reversible formation/decomposition of a ZHT precipitation on the surface of the cathode during the cycling, resulting in an additional increase in capacity. The composite cathode of pp-fibers@VO_2(B) delivers a high specific capacity of 491 mAh g^{-1} at a specific current of 0.2 A g^{-1} and a superior rate capability of 140 mAh g^{-1} at 10.0 A g^{-1}. In addition, the maximum energy and power densities of the prepared ZIBs were 378 and 11 kW kg^{-1}, respectively (based on the mass of the cathode). Furthermore, the assembled soft-packed Zn//pp-fibers@VO_2(B) pouch cells show excellent flexibility and stable electrochemical performance under various bending states, which could be a promising candidate for portable and wearable power sources.

ACKNOWLEDGMENTS

This research was supported by "Regional Innovation Strategy (RIS)" through the National Research Foundation of Korea (NRF) funded by the Ministry of Education (MOE) (2021RIS-001). It was also supported by National Research Foundation (NRF) funded by the Ministry of Science and Technology (NRF-2021R1F1A1064111) and Ministry of Education (NRF-2017R1A6A1A06015181) of the Republic of Korea.

CONFLICT OF INTEREST STATEMENT

The authors declare that there are no conflicts of interests.

ORCID

Yeonho Kim http://orcid.org/0000-0002-6004-4975
Ho Seok Park http://orcid.org/0000-0002-4424-4037

REFERENCES

1. Song M, Tan H, Chao D, Fan HJ. Recent advances in Zn-ion batteries. *Adv Funct Mater*. 2018;28(41):1802564.
2. Goodenough JB, Park K-S. The Li-ion rechargeable battery: a perspective. *J Am Chem Soc*. 2013;135(4):1167-1176.
3. Wang D, Li Q, Zhao Y, et al. Insight on organic molecules in aqueous Zn-ion batteries with an emphasis on the Zn anode regulation. *Adv Energy Mater*. 2022;12(9):2102707.
4. Zampardi G, La Mantia F. Open challenges and good experimental practices in the research field of aqueous Zn-ion batteries. *Nat Commun*. 2022;13:687.
5. Ming J, Guo J, Xia C, Wang W, Alshareef HN. Zinc-ion batteries: materials, mechanisms, and applications. *Mater Sci Eng R Rep*. 2019;135:58-84.
6. Zhang L, Chen L, Zhou X, Liu Z. Towards high-voltage aqueous metal-ion batteries beyond 1.5 V: the zinc/zinc hexacyanoferrate system. *Adv Energy Mater*. 2015;5(2):1400930.
7. Kundu D, Adams BD, Duffort V, Vajargah SH, Nazar LF. A high-capacity and long-life aqueous rechargeable zinc battery using a metal oxide intercalation cathode. *Nat Energy*. 2016;1(10):16119.
8. Trócoli R, La Mantia F. An aqueous zinc-ion battery based on copper hexacyanoferrate. *ChemSusChem*. 2015;8(3):481-485.

9. Li C, Jin S, Archer LA, Nazar LF. Toward practical aqueous zinc-ion batteries for electrochemical energy storage. *Joule*. 2022;6(8):1733-1738.
10. Liu H, Hou X, Fang T, et al. Boosting zinc-ion storage in hydrated vanadium oxides via migration regulation. *Energy Storage Mater*. 2023;55:279-288.
11. Ding J, Du Z, Gu L, et al. Ultrafast Zn^{2+} intercalation and deintercalation in vanadium dioxide. *Adv Mater*. 2018;30(26): 1800762.
12. Liu S, He J, Liu D, et al. Suppressing vanadium dissolution by modulating aqueous electrolyte structure for ultralong life-span zinc ion batteries at low current density. *Energy Stor Mater*. 2022;49:93-101.
13. Mathew V, Sambandam B, Kim S, et al. Manganese and vanadium oxide cathodes for aqueous rechargeable zinc-ion batteries: a focused view on performance, mechanism, and developments. *ACS Energy Lett*. 2020;5(7):2376-2400.
14. Zhang Y, Lu L, Chen Y, et al. Polydopamine modification of silk fibroin membranes significantly promotes their wound healing effect. *Biomater Sci*. 2019;7(12):5232-5237.
15. Kong J, Yee WA, Yang L, et al. Highly electrically conductive layered carbon derived from polydopamine and its functions in SnO_2-based lithium ion battery anodes. *Chem Commun*. 2012;48(83):10316-10318.
16. Chaudhari KN, Rajeev KK, Kim S, et al. Performance enhancement of carbon-coated Si nanoparticles for lithium-ion batteries through the generation of lithophilic sites by a simple oxidation process. *Appl Surf Sci*. 2022;602(15):154361.
17. Tamilselvan M, Sreekanth TVM, Yoo K, Kim J. Binder-free coaxially grown V_6O_{13} nanobelts on carbon cloth as cathodes for highly reversible aqueous zinc ion batteries. *Appl Surf Sci*. 2020;529(1):147077.
18. Shi Y, Zhou X, Yu G. Material and structural design of novel binder systems for high-energy, high-power lithium-ion batteries. *Acc Chem Res*. 2017;50(11):2642-2652.
19. Zhang Z, Zeng T, Lai Y, Jia M, Li J. A comparative study of different binders and their effects on electrochemical properties of $LiMn_2O_4$ cathode in lithium ion batteries. *J Power Sources*. 2014;247(1):1-8.
20. Choi N-S, Ha S-Y, Lee Y, et al. Recent progress on polymeric binders for silicon anodes in lithium-ion batteries. *J Electrochem Sci Technol*. 2015;6(2):35-49.
21. Wu M, Zhang G, Chen N, Chen W, Qiao J, Sun S. A self-supported electrode as a high-performance binder- and carbon-free cathode for rechargeable hybrid zinc batteries. *Energy Storage Mater*. 2020;24:272-280.
22. Zhou S, Wang M, Yang Z, Zhang X. Polydopamine-modified nanochannels in vertically aligned carbon nanotube arrays for controllable molecule transport. *ACS Appl Nano Mater*. 2019;2(5):3271-3279.
23. Liu D, Zhang Q, Chen X, et al. Microstructure modulation of Zn doped VO_2(B) nanorods with improved electrochemical properties towards high performance aqueous batteries. *Batteries*. 2022;8(10):172.
24. Zhu P, Gastol D, Marshall J, Sommerville R, Goodship V, Kendrick E. A review of current collectors for lithium-ion batteries. *J Power Sources*. 2021;485(15):229321.
25. Wen YH, Shao L, Zhao PC, Wang BY, Cao GP, Yang YS. Carbon coated stainless steel mesh as a low-cost and corrosion-resistant current collector for aqueous rechargeable batteries. *J Mater Chem A*. 2017;5(30):15752-15758.
26. Wang L, Huang K-W, Chen J, Zheng J. Ultralong cycle stability of aqueous zinc-ion batteries with zinc vanadium oxide cathodes. *Sci Adv*. 2019;5(10):eaax4279.
27. Yan M, He P, Chen Y, et al. Water-lubricated intercalation in $V_2O_5{\cdot}nH_2O$ for high-capacity and high-rate aqueous rechargeable zinc batteries. *Adv Mater*. 2018;30(1):1703725.
28. Geng H, Cheng M, Wang B, Yang Y, Zhang Y, Li CC. Electronic structure regulation of layered vanadium oxide via interlayer doping strategy toward superior high-rate and low-temperature zinc-ion batteries. *Adv Funct Mater*. 2020;30(6):1907684.
29. Pan H, Shao Y, Yan P, et al. Reversible aqueous zinc/manganese oxide energy storage from conversion reactions. *Nat Energy*. 2016;1(5):16039.
30. Zhou J, Shan L, Wu Z, Guo X, Fang G, Liang S. Investigation of V_2O_5 as a low-cost rechargeable aqueous zinc ion battery cathode. *Chem Commun*. 2018;54(35):4457-4460.
31. Xia C, Guo J, Lei Y, Liang H, Zhao C, Alshareef HN. Rechargeable aqueous zinc-ion battery based on porous framework zinc pyrovanadate intercalation cathode. *Adv Mater*. 2018;30(5):1705580.
32. Park J-S, Jo JH, Aniskevich Y, et al. Open-structured vanadium dioxide as an intercalation host for Zn ions: investigation by first-principles calculation and experiments. *Chem Mater*. 2018;30(19):6777-6787.
33. Liao M, Wang J, Ye L, et al. A deep-cycle aqueous zinc-ion battery containing an oxygen-deficient vanadium oxide cathode. *Angew Chem*. 2020;132(6):2293-2298.
34. He P, Zhang G, Liao X, et al. Sodium ion stabilized vanadium oxide nanowire cathode for high-performance zinc-ion batteries. *Adv Energy Mater*. 2018;8(10):1702463.
35. Xu D, Wang H, Li F, et al. Conformal conducting polymer shells on V_2O_5 nanosheet arrays as a high-rate and stable zinc-ion battery cathode. *Adv Mater Interfaces*. 2019;6(2):1801506.
36. Yang G, Li Q, Ma K, Hong C, Wang C. The degradation mechanism of vanadium oxide-based aqueous zinc-ion batteries. *J Mater Chem A*. 2020;8(16):8084-8095.
37. Oberholzer P, Tervoort E, Bouzid A, Pasquarello A, Kundu D. Oxide versus nonoxide cathode materials for aqueous Zn batteries: an insight into the charge storage mechanism and consequences thereof. *ACS Appl Mater Interfaces*. 2018;11(1):674-682.
38. Wang X, Ma L, Sun J. Vanadium pentoxide nanosheets in-situ spaced with acetylene black as cathodes for high-performance zinc-ion batteries. *ACS Appl Mater Interfaces*. 2019;11(44): 41297-41303.
39. Liu W, Dong L, Jiang B, et al. Layered vanadium oxides with proton and zinc ion insertion for zinc ion batteries. *Electrochim Acta*. 2019;320(10):134565.
40. Dong Y, Jia M, Wang Y, et al. Long-life zinc/vanadium pentoxide battery enabled by a concentrated aqueous $ZnSO_4$ electrolyte with proton and zinc ion co-intercalation. *ACS Appl Energy Mater*. 2020;3(11):11183-11192.
41. Liu L, Wu YC, Huang L, et al. Alkali ions pre-intercalated layered MnO_2 nanosheet for zinc-ions storage. *Adv Energy Mater*. 2021;11(31):2101287.
42. Hu P, Zhu T, Wang X, et al. Aqueous Zn//$Zn(CF_3SO_3)_2$//$Na_3V_2(PO_4)_3$ batteries with simultaneous Zn^{2+}/Na^+ intercalation/de-intercalation. *Nano Energy*. 2019;58:492-498.

43. Chen X, Wang L, Li H, Cheng F, Chen J. Porous V_2O_5 nanofibers as cathode materials for rechargeable aqueous zinc-ion batteries. *J Energy Chem*. 2019;38:20-25.
44. Chao D, Zhu C, Song M, et al. A high-rate and stable quasi-solid-state zinc-ion battery with novel 2D layered zinc orthovanadate array. *Adv Mater*. 2018;30(32):1803181.
45. Lindström H, Södergren S, Solbrand A, et al. Li^+ ion insertion in TiO_2 (Anatase). 2. Voltammetry on nanoporous films. *J Phys Chem B*. 1997;101(39):7717-7722.
46. Liu J, Wang J, Xu C, et al. Advanced energy storage devices: basic principles, analytical methods, and rational materials design. *Adv Sci*. 2018;5(1):1700322.
47. Yu X, Yun S, Yeon JS, et al. Emergent pseudocapacitance of 2D nanomaterials. *Adv Energy Mater*. 2018;8(13):1702930.
48. Yeon JS, Park TH, Ko YH, et al. 2D spinel $ZnCo_2O_4$ microsheet-coated functional separator for promoted redox kinetics and inhibited polysulfide dissolution. *J Energy Chem*. 2021;55:468-475.
49. Chen L, Yang Z, Huang Y. Monoclinic VO_2(D) hollow nanospheres with super-long cycle life for aqueous zinc ion batteries. *Nanoscale*. 2019;11(27):13032-13039.
50. Cao Z, Wang L, Zhang H, et al. Localized Ostwald ripening guided dissolution/regrowth to ancient Chinese coin-shaped VO_2 nanoplates with enhanced mass transfer for zinc ion storage. *Adv Funct Mater*. 2020;30(25):2000472.
51. Liu Y, Hu P, Liu H, Wu X, Zhi C. Tetragonal VO_2 hollow nanospheres as robust cathode material for aqueous zinc ion batteries. *Mater Today Energy*. 2020;17:100431.
52. Kang MS, Park SK, Nakhanivej P, Shin KH, Yeon JS, Park HS. Mesoporous VO_2(B) nanorods deposited onto graphene architectures for enhanced rate capability and cycle life of Li ion battery cathodes. *J Alloys Compd*. 2021;855(25):157361.
53. Liu S, Kang L, Hu J, et al. Realizing superior redox kinetics of hollow bimetallic sulfide nanoarchitectures by defect-induced manipulation toward flexible solid-state supercapacitors. *Small*. 2022;18(5):2104507.
54. Liu S, Kang L, Hu J, et al. Unlocking the potential of oxygen-deficient copper-doped Co_3O_4 nanocrystals confined in carbon as an advanced electrode for flexible solid-state supercapacitors. *ACS Energy Lett*. 2021;6(9):3011-3019.
55. Liu S, Yin Y, Hui KS, Hui KN, Lee SC, Jun SC. High-performance flexible quasi-solid-state supercapacitors realized by molybdenum dioxide@nitrogen-doped carbon and copper cobalt sulfide tubular nanostructures. *Adv Sci*. 2018;5(10):1800733.
56. Liu S, Kang L, Zhang J, Jung E, Lee S, Jun SC. Structural engineering and surface modification of MOF-derived cobalt-based hybrid nanosheets for flexible solid-state supercapacitors. *Energy Storage Mater*. 2020;32:167-177.

SUPPORTING INFORMATION

Additional supporting information can be found online in the Supporting Information section at the end of this article.

How to cite this article: Yeon JS, Park SK, Kim S, et al. Self-supported VO_2 on polydopamine-derived pyroprotein-based fibers for ultrastable and flexible aqueous zinc-ion batteries. *Carbon Energy*. 2024;e469. doi:10.1002/cey2.469